

Article

Fractional Differential Equation Physics-Informed Neural Network and Its Application in Battery State Estimation

Lujuan Dang ^{1*} and Zilai Wang ¹

¹ School of Artificial Intelligence, Xi'an Jiaotong University, Xi'an 710049, China

* Correspondence: danglj@xjtu.edu.cn

Abstract

Accurate estimation of the State of Charge (SOC) is critical for ensuring the safety, reliability, and performance optimization of lithium-ion battery systems. Conventional data-driven neural network models often struggle to fully characterize the inherent complex nonlinearities and memory-dependent dynamics of electrochemical processes, significantly limiting their predictive accuracy and physical interpretability under dynamic operating conditions. To address this challenge, this study proposes a novel neural architecture termed the Fractional Differential Equation Physics-Informed Neural Network (FDIFF-PINN), which integrates fractional calculus with deep learning. The main contributions of this paper include: (1) Based on a fractional-order equivalent circuit model, a discretized fractional-order partial differential equation is constructed. We propose embedding the residual term of the fractional-order dynamic equation into the loss function of a neural network as a physical regularization constraint, thereby integrating the mechanistic model with a deep learning architecture. This dual-driven paradigm retains the data-driven model's ability to represent high-dimensional features while capturing the battery's non-ideal polarization behavior and historical dependencies by incorporating the long-range temporal correlation prior knowledge embedded within the fractional-order differential operator. This significantly enhances the physical consistency of the model for battery SOC estimation, providing a novel solution for high-accuracy, high-robustness battery state estimation. (2) Comparative experiments were conducted using a dynamic charge/discharge dataset of Panasonic 18650PF batteries under multi-temperature conditions (from -10°C to 20°C). The performance of the FDIFF-PINN method was validated across various operating conditions, physical weighting coefficients, initial weight settings, and fractional-order parameters. Parameter tuning was performed under specific conditions. Results demonstrate that the proposed hybrid modeling method exhibits significant improvement over traditional data-driven methods under low-temperature and steady-state conditions, with the Mean Squared Error stabilized below 3% under specific operating conditions. The experiment, utilizing modeling with a single-parameter operator, verifies the excellent fitting capability of fractional-order equivalent circuit modeling for practical electrochemical systems.

Keywords: Differential equation-informed neural networks; State estimation; State of charge (SOC); Fractional order RC equivalent circuit model

1. Introduction

1.1. Research Background and Basic Concepts

As the global energy structure undergoes deep adjustment and carbon neutrality goals are advanced, the energy industry is transitioning from a traditional fossil-fuel-dominated system to a clean, intelligent, and sustainable architecture. Due to technological advancements, decarbonization initiatives, the establishment of smart grid concepts, and the rapid growth in renewable resource usage, energy concepts are evolving worldwide. With the increasing global demand for power generation and

the widespread use of diesel, gasoline, and various fossil fuels leading to greenhouse gas emissions like carbon dioxide and global warming, nations are planning to reduce carbon emissions to achieve carbon neutrality and expand the use of new energy. Lithium-ion batteries, due to their high energy density, long cycle life, and low self-discharge rate, have become the core energy storage carriers for electric vehicles (EVs), renewable energy systems, and portable electronic devices [1,2].

Batteries rarely operate under ideal conditions; their performance is influenced by temperature fluctuations, repeated charge/discharge cycles, aging processes, and operating stresses. These factors make it difficult to accurately assess the internal state of the battery without sophisticated estimation processes, which are crucial for monitoring battery performance and predicting behavior under dynamic environments. Key parameters for battery state estimation include: State of Charge (SOC), quantifying remaining energy capacity relative to total capacity; State of Health (SOH), assessing overall aging and capacity fade; and Remaining Useful Life (RUL), predicting the life termination threshold. Failure to accurately estimate these key parameters makes efficient battery management impossible, potentially triggering abnormal conditions such as overcharge, deep discharge, or overheating. These failure modes not only significantly shorten battery cycle life but may also induce catastrophic consequences like thermal runaway in extreme cases, directly threatening system safety.

Therefore, accurate prediction and prevention of lithium battery safety risks are important guarantees for improving battery safety and reliability and have become an international research hotspot. A high-performance Battery Management System (BMS) is crucial for ensuring lithium battery safety. As the key to safe and efficient battery operation, the BMS undertakes real-time monitoring and control of battery status, among which accurate SOC estimation is particularly important. SOC is defined as the ratio of the battery's current available charge to its rated capacity, serving as the basis for assessing remaining energy and predicting range. However, due to complex physical factors such as nonlinear characteristics during charge/discharge, temperature effects, internal resistance changes, and aging effects, accurate SOC estimation faces multiple challenges. Thus, developing SOC estimation methods that balance high accuracy and strong robustness is a core task of modern BMS research. Currently, common SOC estimation methods include model-based methods and data-driven methods.

1.2. Current Status of Model-Based SOC Estimation Methods

Model-driven SOC estimation methods are primarily categorized into three types: Ampere-hour integration, Open Circuit Voltage (OCV) method, and state observer methods based on Equivalent Circuit Models (ECM). The Ampere-hour integration method calculates SOC changes by accumulating charge/discharge currents. Although simple, it suffers from dependence on initial SOC accuracy and accumulation of current measurement errors. Plett et al. [1,2] showed that after 100 hours of continuous operation, a 0.5% current measurement error can lead to an SOC estimation deviation exceeding 8%. The OCV method uses the correspondence between SOC and equilibrium potential but requires long resting times, failing to meet real-time requirements.

To overcome these limitations, model-based technical paths have become important for high-precision SOC estimation. These methods construct a mathematical representation of the battery, correlating external measurable parameters (voltage, current, temperature) with internal electrochemical processes to form a closed-loop estimation system. The core mechanism involves correcting internal states of a filter or observer through the residual feedback between measured and model-predicted voltages.

Representative methods include macroscopic characterization using ECMs and microscopic modeling based on electrochemical mechanisms. ECMs construct equivalent circuit networks to simulate battery external characteristics using ideal components like resistors and capacitors. While computationally efficient, they lack the ability to describe key internal states like electrode overpotential and solid-phase concentration distribution. Hu et al. [3] compared different ECMs, noting that the second-order RC model achieves a good balance between accuracy and computation.

To break through ECM limitations, the Pseudo-Two-Dimensional (P2D) model based on multi-physics coupling was introduced. It accurately depicts internal electrochemical behavior by solving complex partial differential equations but entails a massive computational load, making it difficult for real-time BMS applications. The Extended Single Particle (SP2) model was proposed as a compromise, reducing complexity while retaining necessary electrochemical features.

Fractional-order models originate from fractional calculus theory. In battery modeling, traditional integer-order models cannot accurately describe non-integer order dynamic characteristics like diffusion and double-layer effects. Researchers introduced fractional calculus, using Constant Phase Elements (CPE) to replace capacitors, better fitting physical mechanisms. Fractional models offer advantages in dynamic characterization (capturing memory effects), flexibility (fractional order as a degree of freedom), data adaptability, and describing "memory" and "heredity" characteristics.

Table 1 summarizes the pros and cons of different model-based SOC estimation methods.

Table 1. Advantages and Disadvantages of SOC Estimation Methods Based on Different Models.

Model	Disadvantages	Advantages
First-order ECM	Lower accuracy; poor dynamic description.	Simple, few parameters, low computation.
Second-order ECM	Increased complexity; parameter ID difficult.	Accurate polarization description; higher accuracy.
Fractional-order	High complexity; calculation heavy.	Precise dynamic/memory description; high SOC accuracy.
Electrochemical	Complex; relies on parameter ID.	Based on internal mechanism; accurate state description.
P2D Model	PDE solution required; huge computation.	Very accurate characteristic description.
SP2 Model	Simplifications limit complete description.	Balance of accuracy/efficiency; good for real-time.

In state estimation algorithms, Kalman filtering is the benchmark. Extended Kalman Filter (EKF) uses local linearization, while Adaptive EKF (AEKF) estimates noise covariance online [19,20]. Unscented Kalman Filter (UKF) uses deterministic sampling to avoid Jacobian calculations, improving accuracy. Methods combining Recursive Least Squares (RLS) with adaptive filtering, like FFRLS-AUKF [21], further advance the field. Seaman et al. [4] integrated impedance spectroscopy into ECM, improving dynamic adaptability. However, these methods rely on extensive data for parameter identification, and integer-order equations struggle to describe fractional-order dynamics of the electrode interface.

1.3. Current Status of Data-Driven SOC Estimation Methods

Data-driven SOC estimation methods, including Multi-Layer Perceptron (MLP) [6], Support Vector Machine (SVM), Random Forest (RF), Recurrent Neural Network (RNN) [7], and Long Short-Term Memory (LSTM) [8], are rising. These methods automatically learn nonlinear mappings from historical data. While they can reduce error to within 2% in standard tests, they suffer from poor interpretability, data dependence, and sensitivity to noise.

Chen et al. [6] achieved 2.1% error with MLP under constant current, but error surged in dynamic conditions. Li et al. [7] combined Elman NN with LSTM to reduce dynamic error. Wang et al. [8] used SVR for robust estimation against noise. However, purely data-driven methods assume training and test data follow the same distribution, which is often invalid due to dynamic degradation and varying operating conditions.

Transfer learning and ensemble learning have been applied to address these issues. Tang et al. [22] and Tan et al. [23] used transfer learning for aging trajectory and state estimation. Shen et al. [24] combined transfer learning with CNNs. Ensemble learning integrates multiple algorithms to improve robustness.

However, these methods share common problems: "Black Box" nature (lack of interpretability), generalization limits (performance drop outside training conditions), and high computational cost (large parameter sets). To fuse physical mechanisms with data, Wang et al. [10] introduced Physics-Informed Neural Networks (PINN) to batteries. Dang et al. [11] coupled electrochemical models with LSTM. Yang's team [13] showed fractional-order models better describe SOC dynamics under attack conditions.

1.4. Structure of the Thesis

Chapter 1 outlines the background. Chapter 2 introduces battery modeling and fractional calculus theory. Chapter 3 elaborates on the FDIFF-PINN architecture and training. Chapter 4 presents experimental results and ablation analysis. Chapter 5 concludes and looks forward to future research.

2. Theoretical Basis of Battery Modeling and Fractional Calculus

2.1. Theoretical Basis of SOC Estimation

SOC is defined as the ratio of current remaining capacity to rated capacity:

$$SOC(t) = \frac{C_{now}}{C_{rated}} \quad (1)$$

In practice, SOC evolution is calculated via current integration (Coulomb counting):

$$SOC(t) = SOC(t_0) - \frac{1}{C_N} \int_{t_0}^t \eta I(\tau) d\tau \quad (2)$$

where η is Coulombic efficiency. SOH characterizes aging:

$$SOH = \frac{Q_{max}}{Q_{initial}} \times 100\% \quad (3)$$

Model-based estimation typically uses state-space equations, such as the Thevenin model:

$$\begin{cases} \dot{U}_p = -\frac{U_p}{R_p C_p} + \frac{I}{C_p} \\ U_t = U_{ocv}(SOC) - U_p - IR_0 \end{cases} \quad (4)$$

EKF is often used for state estimation based on these models.

2.2. Theoretical Basis of Fractional Calculus

Fractional calculus extends integration and differentiation to real orders. The Riemann-Liouville definition for order α is:

$${}_{t_0} D_t^\alpha f(t) = \frac{1}{\Gamma(n-\alpha)} \frac{d^n}{dt^n} \int_{t_0}^t (t-\tau)^{n-\alpha-1} f(\tau) d\tau \quad (5)$$

The Caputo definition exchanges differentiation and integration orders. The Grünwald-Letnikov (GL) definition is useful for numerical implementation. Fractional derivatives exhibit non-locality and memory effects, making them suitable for modeling electrochemical processes like diffusion [17,18].

2.3. Fractional Differential Equation Modeling of Battery System Dynamics

2.3.1. Mathematical Basis and Battery Modeling

Fractional differentiation captures memory effects inherent in battery electrode charge transport. The GL definition allows discrete approximation:

$$D_t^\alpha x(t) \approx \frac{1}{T^\alpha} \sum_{j=0}^M w_j^{(\alpha)} x(t - jT) \quad (6)$$

where $w_j^{(\alpha)}$ are generalized binomial coefficients. This form establishes an explicit link between current and historical states.

2.3.2. Constant Phase Element (CPE)

The Constant Phase Element (CPE) describes non-ideal capacitive behavior. Its impedance is:

$$Z_{CPE}(s) = \frac{1}{Qs^\alpha} \quad (7)$$

where α characterizes the fractal nature of the electrode interface. $\alpha = 1$ implies an ideal capacitor, while $\alpha = 0.5$ represents Warburg impedance (diffusion).

2.4. Deep Learning Based SOC Estimation Methods

2.4.1. Multilayer Perceptron (MLP)

MLP is a feedforward network. For SOC estimation, it maps inputs $U(t), I(t), T(t)$ to $SOC(t)$. However, it lacks time-series memory and requires sliding windows, leading to high parameter counts and lack of physical interpretability.

2.4.2. Recurrent Neural Network (RNN)

RNN introduces hidden states $H(t)$ to memorize history. However, it suffers from gradient vanishing/exploding problems during backpropagation over long sequences, limiting its ability to capture long-term dependencies in battery dynamics.

2.4.3. Long Short-Term Memory (LSTM)

LSTM addresses RNN limitations using gating mechanisms (Forget, Input, Output gates) and a cell state $C(t)$ to maintain information flow. It is effective for time-series but remains a black-box model.

2.5. Summary

This chapter established the theoretical foundation for fusing fractional physics with deep learning. Fractional calculus naturally describes battery memory effects, while deep learning offers powerful fitting. Integrating them addresses the physical inconsistency of pure data models.

3. Application of FDIFF-PINN in SOC Estimation

3.1. Model Architecture and Formula Definition

We adopt a battery model based on the Grünwald-Letnikov (G-L) fractional derivative to describe memory effects. **SOC Dynamics Equation:**

$$\frac{d^\alpha SOC(t)}{dt^\alpha} = -\frac{\eta I(t)}{C_n} \quad (8)$$

Polarization Voltage Equation:

$$C_p \frac{d^\alpha U_p(t)}{dt^\alpha} + \frac{U_p(t)}{R_p} = I(t) \quad (9)$$

Terminal Voltage Equation:

$$U_t(t) = U_{ocv}(SOC(t)) - I(t)R_0 - U_p(t) \quad (10)$$

3.2. Discretization Implementation Method

We use the G-L formula for discretization:

$$D_t^\alpha x(t) \approx \frac{1}{T_s^\alpha} \sum_{j=0}^M w_j^{(\alpha)} x(t - jT_s) \quad (11)$$

where $w_j^{(\alpha)} = (-1)^j j^{(\alpha)}$. This weighted sum of history captures the memory effect.

3.3. Loss Function Design

The loss function includes a data matching term and a physical constraint term. **Data Matching Term (L_{data}):**

$$L_{data} = \frac{1}{N} \sum (SOC_{pred} - SOC_{true})^2 \quad (12)$$

Physical Constraint Term (L_{phy}): This term enforces the fractional differential equations.

$$L_{phy} = L_{dyn} + L_{pol} \quad (13)$$

where L_{dyn} is the residual of the SOC dynamics equation, and L_{pol} is the residual of the polarization voltage equation calculated using the G-L approximation. **Total Loss:**

$$L_{total} = L_{data} + \lambda L_{phy} \quad (14)$$

where λ is a weighting coefficient.

3.4. Training Process

The training uses gradient descent (Adam). Steps: 1. Forward calculation of SOC and U_p . 2. Update history buffer. 3. Calculate fractional derivatives using G-L. 4. Compute residuals L_{phy} . 5. Backpropagate total loss to update weights.

4. Experimental Setup and Result Analysis

To comprehensively validate the effectiveness and superiority of the proposed Fractional Differential Equation Physics-Informed Neural Network (FDIFF-PINN) in battery SOC estimation, this chapter systematically elaborates on the detailed experimental setup and conducts an in-depth analysis of the results. The core objectives of the experiment are: 1) to evaluate the model's prediction accuracy under severe conditions covering various typical driving cycles and operating temperatures; 2) to test the model's generalization ability across different cycles and temperature scenarios; 3) to conduct ablation studies (smiling experiments) on the model to examine the impact of different model parameters on prediction performance. To this end, this chapter first introduces the dataset used in the experiment, the definition of the network model output, and the quantitative evaluation metrics, followed by the description of the data partition strategy. Finally, based on detailed experimental results, a multi-dimensional analysis is performed to provide objective and strong evidence for the performance of the proposed method.

4.1. Experimental Setup

4.1.1. Dataset

This experiment utilizes the LG18650-HG2 lithium-ion battery dataset publicly released by Dr. Phillip Kollmeyer's team at McMaster University, Canada. The dataset includes five standardized dynamic driving cycles:

- **UDDS (Urban Dynamometer Driving Schedule):** Simulates low-frequency urban road conditions with frequent stops and starts.
- **HWFET (Highway Fuel Economy Test):** Represents steady-state highway driving scenarios.

- **LA92 (Los Angeles 92 Cycle):** Reflects a mixed driving mode with medium-speed variable conditions.
- **NN (New York-Newark mixed cycle):** Covers power fluctuations under complex traffic flows.
- **US06 (Supplemental Federal Test Procedure):** Contains extreme power demands with high-frequency rapid acceleration/deceleration.

To evaluate the model's thermal robustness, four key temperature test points are set (-20°C , -10°C , 0°C , $+10^{\circ}\text{C}$), covering the typical operating temperature range of electric vehicles as well as extreme low-temperature environments. The original data sampling frequency is 1Hz, and it is input into the network after sliding window processing. Using different types of charge and discharge datasets can fully verify the effectiveness and generalization of the proposed method.

4.1.2. Network Model Output and Evaluation Metrics

1) Model Output

The output of the network model is the Battery State of Charge (SOC), the core calculation of which is based on the principle of current-time integration, as follows:

$$SOC(t) = SOC(t_0) - \frac{1}{C_N} \int_{t_0}^t \eta I(\tau) d\tau \quad (15)$$

where: t_0 is the initial time point; $SOC(t_0)$ is the initial SOC value generated by random sampling; $SOC(t)$ is the state of charge at time t ; $\eta = 0.999$ is the coulombic efficiency; $I(\tau)$ is the battery current at time τ ; C_N is the rated capacity under different operating conditions.

2) Evaluation Metrics

Common evaluation metrics in experiments include Mean Squared Error (MSE), Root Mean Square Error (RMSE), Mean Absolute Error (MAE), Mean Absolute Percentage Error (MAPE), Symmetric Mean Absolute Percentage Error (SMAPE), and relative errors. This experiment adopts the following metrics, calculated as follows:

$$MAE = \frac{1}{n} \sum_{i=1}^n |y_i - \hat{y}_i| \quad (16)$$

$$MSE = \frac{1}{n} \sum_{i=1}^n (y_i - \hat{y}_i)^2 \quad (17)$$

$$RMSE = \sqrt{\frac{1}{n} \sum_{i=1}^n (y_i - \hat{y}_i)^2} \quad (18)$$

where y_i is the standard value of the i -th cycle, and \hat{y}_i is the estimated value of the i -th cycle. These evaluation metrics have different focuses: MSE gives higher penalties to larger errors, thus making it sensitive to outliers; MAE is less affected by outliers and is more suitable for cases insensitive to outliers. Relative error provides sample-level error analysis, often used for visual assessment and fine-grained analysis.

4.1.3. Dataset Partitioning and Comparison Methods

To verify the generalization ability of the model across cycles and temperatures, this study designed five experimental cases (Case 1–Case 5). The data partitioning strategy is shown in Table 2. The training and testing phases of all cases cover the same temperature range (-20°C , -10°C , 0°C , $+10^{\circ}\text{C}$), with differences mainly in the combination of driving cycles. During the training process, four different batteries are used for training or validation each time, and one is used for testing.

Table 2. Dataset Partitioning.

Experiment	Condition	Temperature (°C)	Driving Cycle
Experiment 1	Training	{ -20, -10, 0, +10}	CC-CV (3A)
	Testing	{ -20, -10, 0, +10}	HWFET
Experiment 2	Training	{ -20, -10, 0, +10}	NN, HWFET, UDDS, US06
	Testing	{ -20, -10, 0, +10}	LA92
Experiment 3	Training	{ -20, -10, 0, +10}	HWFET, LA92, UDDS, US06
	Testing	{ -20, -10, 0, +10}	NN
Experiment 4	Training	{ -20, -10, 0, +10}	HWFET, LA92, NN, US06
	Testing	{ -20, -10, 0, +10}	UDDS
Experiment 5	Training	{ -20, -10, 0, +10}	HWFET, LA92, UDDS, NN
	Testing	{ -20, -10, 0, +10}	US06

The above partition ensures a comprehensive evaluation of the model in diverse dynamic load scenarios by systematically rotating test cycles, avoiding overfitting caused by a single driving mode. In this experiment, Recurrent Neural Network (RNN), Long Short-Term Memory Network (LSTM), and Multi-Layer Perceptron (MLP) were selected as comparison methods, while neural networks coupled with fractional differential equations (FDIFF-PINN-RNN / FDIFF-PINN-LSTM / FDIFF-PINN-MLP) served as the experimental methods. All six methods use the same input data. Models using the same neural network architecture are trained together to minimize training overhead by sharing data. For RNN and LSTM, data is input in groups of sequences set to 20. Other model parameters are kept as identical as possible.

4.2. Experimental Results Analysis

4.2.1. Experimental Results under Different Operating Conditions

1) HWFET Cycle

Table 3 and Table 4 show the performance differences between traditional neural networks and fractional differential equation physics-informed neural networks under the HWFET cycle.

Table 3. Analysis of Neural Network Results under HWFET Cycle.

Method/Temp	MLP		RNN		LSTM	
	MAE	MSE	MAE	MSE	MAE	MSE
-20°C	0.108	0.014	0.338	0.148	0.377	0.176
-10°C	0.814	0.663	0.346	0.165	0.349	0.167
0°C	0.080	0.007	0.079	0.007	0.117	0.0174
10°C	0.150	0.028	0.159	0.031	0.125	0.019

Table 4. Analysis of FDIFF-PINN Results under HWFET Cycle.

Method/Temp	FDIFF-PINN-MLP		FDIFF-PINN-RNN		FDIFF-PINN-LSTM	
	MAE	MSE	MAE	MSE	MAE	MSE
-20°C	0.071	0.006	0.160	0.034	0.329	0.142
-10°C	0.326	0.151	0.361	0.162	0.387	0.192
0°C	0.072	0.006	0.094	0.013	0.094	0.012
10°C	0.138	0.024	0.121	0.023	0.120	0.020

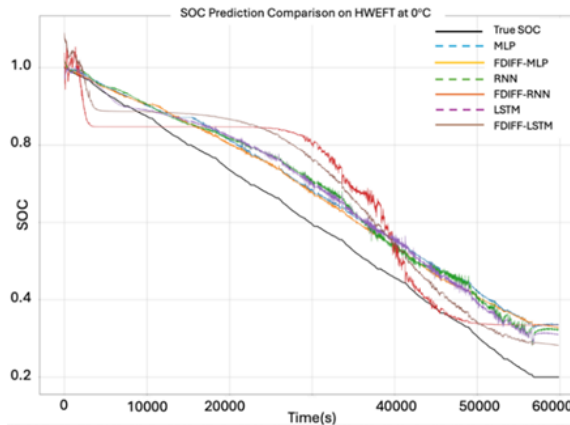


Figure 1. Predicted values and errors of various neural networks under HWFET at 0°C.

Tables 3 and 4 show significant performance differences under HWFET conditions. At extreme low temperature (-20°C), traditional MLP outperforms RNN and LSTM, while the fusion model FDIFF-PINN-MLP further reduces errors to MAE=0.071 and MSE=0.006, verifying the adaptability improvement of physical constraints in extreme environments. However, at -10°C, traditional MLP degrades significantly, worse than RNN and LSTM. Although FDIFF-PINN-MLP improves upon the traditional method, the magnitude is limited. At 0°C, both types of models reach peak performance; traditional MLP and RNN have MAEs below 0.08, while fusion models mitigate volatility through balanced improvements. At 10°C, traditional LSTM performs best, but fusion models show more concentrated error distribution, with FDIFF-PINN-MLP still outperforming traditional MLP.

2) LA92 Cycle

Table 5. Analysis of Neural Network Results under LA92 Cycle.

Method/Temp	MLP		RNN		LSTM	
	MAE	MSE	MAE	MSE	MAE	MSE
-20°C	0.195	0.055	0.161	0.035	0.246	0.089
-10°C	0.186	0.045	0.185	0.046	0.182	0.044
0°C	0.306	0.123	0.264	0.106	0.237	0.091
10°C	0.284	0.117	0.226	0.069	0.286	0.119

Table 6. Analysis of FDIFF-PINN Results under LA92 Cycle.

Method/Temp	FDIFF-PINN-MLP		FDIFF-PINN-RNN		FDIFF-PINN-LSTM	
	MAE	MSE	MAE	MSE	MAE	MSE
-20°C	0.167	0.038	0.160	0.034	0.229	0.077
-10°C	0.186	0.046	0.186	0.046	0.104	0.014
0°C	0.210	0.059	0.211	0.059	0.212	0.061
10°C	0.244	0.083	0.227	0.069	0.295	0.127

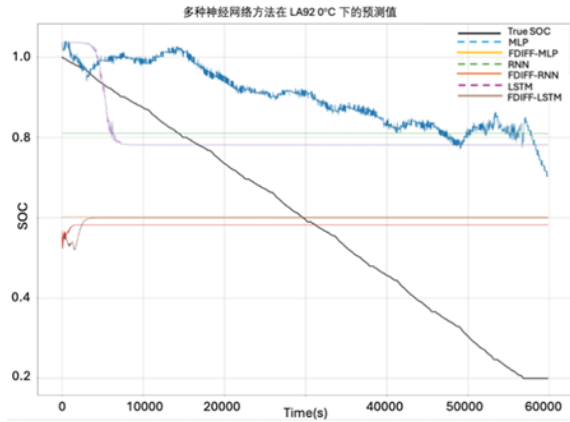


Figure 2. Predicted values and errors of various neural networks under LA92 at 0°C.

Comparing Tables 5 and 6, under LA92 conditions at -20°C, traditional RNN (MAE=0.161, MSE=0.035) outperforms MLP and LSTM. Among fusion models, FDIFF-PINN-RNN (MAE=0.160) is slightly better, and FDIFF-PINN-MLP (MAE=0.167) is significantly better than traditional MLP (0.195). At -10°C, traditional LSTM is best (MAE=0.182), while FDIFF-PINN-LSTM dramatically drops to MAE=0.104, MSE=0.014. At 0°C, traditional LSTM maintains an advantage, but FDIFF-PINN-MLP and FDIFF-PINN-RNN (MAE 0.21) significantly outperform traditional MLP (0.306). At 10°C, traditional RNN performs best; FDIFF-PINN-RNN approaches this level, while FDIFF-PINN-MLP still improves upon traditional MLP.

3) NN Cycle

Table 7. Analysis of Neural Network Results under NN Cycle.

Method/Temp	MLP		RNN		LSTM	
	MAE	MSE	MAE	MSE	MAE	MSE
-20°C	0.177	0.045	0.158	0.033	0.231	0.081
-10°C	0.549	0.306	0.180	0.043	0.186	0.049
0°C	0.157	0.033	0.209	0.058	0.208	0.057
10°C	0.276	0.112	0.203	0.055	0.281	0.116

Table 8. Analysis of FDIFF-PINN Results under NN Cycle.

Method/Temp	FDIFF-PINN-MLP		FDIFF-PINN-RNN		FDIFF-PINN-LSTM	
	MAE	MSE	MAE	MSE	MAE	MSE
-20°C	0.161	0.035	0.236	0.084	0.193	0.056
-10°C	0.180	0.044	0.185	0.049	0.202	0.071
0°C	0.155	0.033	0.209	0.058	0.208	0.058
10°C	0.255	0.095	0.203	0.055	0.329	0.155

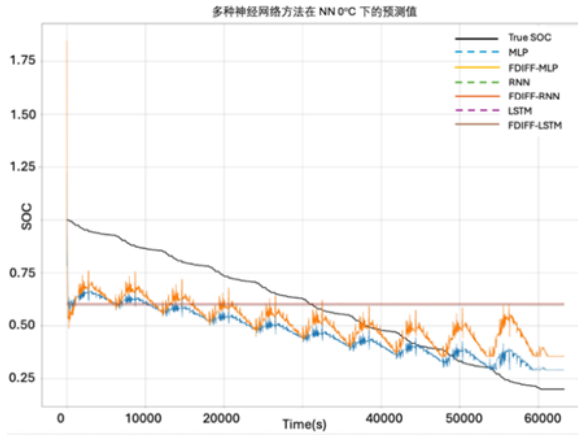


Figure 3. Predicted values and errors of various neural networks under NN at 0°C.

Tables 7 and 8 show that under NN cycle at -20°C, traditional RNN is best (MAE=0.158). FDIFF-PINN-MLP improves on traditional MLP, but FDIFF-PINN-RNN degrades significantly. At -10°C, traditional MLP degrades severely (MAE=0.549), while FDIFF-PINN-MLP improves drastically to 0.180, comparable to RNN/LSTM. At 0°C, traditional MLP is best (MAE=0.157), with FDIFF-PINN-MLP slightly optimizing to 0.155. At 10°C, FDIFF-PINN-LSTM performs significantly worse than traditional LSTM, indicating limitations in adaptability for some models.

4) US06 Cycle

Table 9. Analysis of Neural Network Results under US06 Cycle.

Method/Temp	MLP		RNN		LSTM	
	MAE	MSE	MAE	MSE	MAE	MSE
-20°C	0.166	0.039	0.164	0.032	0.167	0.040
-10°C	0.201	0.044	0.178	0.042	0.112	0.015
0°C	0.485	0.289	0.212	0.060	0.193	0.054
10°C	0.261	0.098	0.223	0.067	0.200	0.050

Table 10. Analysis of FDIFF-PINN Results under US06 Cycle.

Method/Temp	FDIFF-PINN-MLP		FDIFF-PINN-RNN		FDIFF-PINN-LSTM	
	MAE	MSE	MAE	MSE	MAE	MSE
-20°C	3.17	10.6	0.154	0.037	0.174	0.044
-10°C	0.178	0.042	0.179	0.043	0.189	0.047
0°C	0.079	0.009	0.284	0.113	0.182	0.048
10°C	0.260	0.097	0.278	0.113	0.210	0.060

Tables 9 and 10 show that at -20°C, FDIFF-PINN-RNN improves slightly over RNN, but FDIFF-PINN-MLP shows instability (MAE=3.17). At -10°C, traditional LSTM is best. At 0°C, FDIFF-PINN-MLP achieves global optimum with MAE=0.079 (83.7% improvement over MLP), while FDIFF-PINN-RNN degrades. Overall, fusion models can significantly optimize performance under specific temperatures but require high model adaptability.

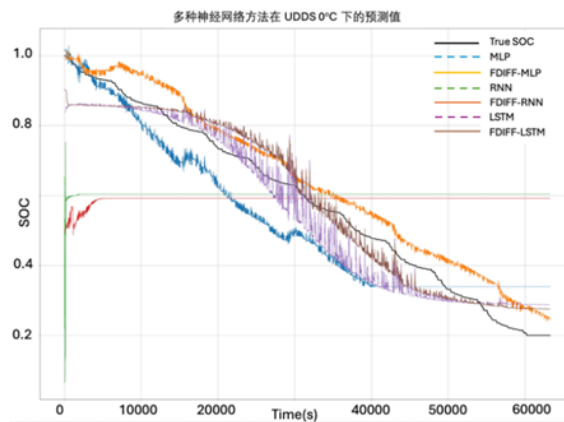
5) UDDS Cycle

Table 11. Analysis of Neural Network Results under UDDS Cycle.

Method/Temp	MLP		RNN		LSTM	
	MAE	MSE	MAE	MSE	MAE	MSE
-20°C	0.158	0.033	0.179	0.047	0.167	0.040
-10°C	0.725	0.549	0.165	0.037	0.112	0.015
0°C	0.179	0.047	0.167	0.040	0.193	0.054
10°C	0.165	0.036	0.174	0.044	0.200	0.050

Table 12. Analysis of FDIFF-PINN Results under UDDS Cycle.

Method/Temp	FDIFF-PINN-MLP		FDIFF-PINN-RNN		FDIFF-PINN-LSTM	
	MAE	MSE	MAE	MSE	MAE	MSE
-20°C	0.167	0.038	0.160	0.034	0.174	0.044
-10°C	0.161	0.035	0.246	0.089	0.189	0.047
0°C	0.160	0.034	0.229	0.077	0.182	0.048
10°C	0.246	0.089	0.186	0.046	0.210	0.060

**Figure 4.** Predicted values and errors of various neural networks under UDDS at 0°C.

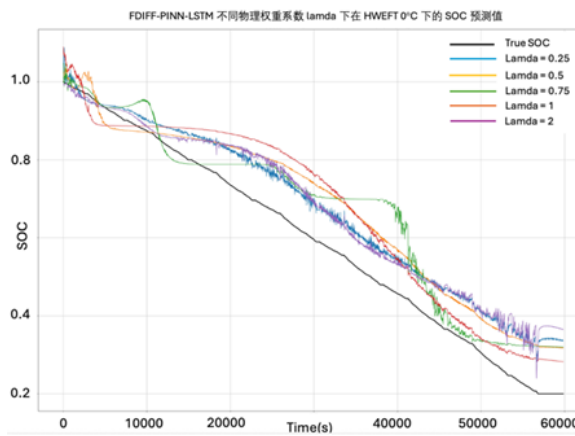
Tables 11 and 12 indicate that at -20°C, FDIFF-PINN-RNN slightly outperforms standard RNN. At -10°C, FDIFF-PINN-MLP significantly improves upon the degraded standard MLP (MAE 0.725 vs 0.161). At 0°C, FDIFF-PINN-MLP further optimizes performance. Overall, FDIFF-PINN shows significant advantages in low-temperature conditions (e.g., -20°C HWFET, MAE reduced by 33.7%), but exhibits condition-dependent advantages in high temperatures and potential instability in complex conditions (US06).

4.2.2. Impact of Physical Weighting Coefficient

The physical weighting coefficient λ adjusts the coupling strength between the data-driven model and the physical mechanism model. Table 13 shows the performance of MLP, RNN, and LSTM with λ varying in $[0, 2]$.

Table 13. Analysis of FDIFF-PINN Results under Different Physical Weighting Coefficients.

Lambda	FDIFF-PINN-MLP		FDIFF-PINN-RNN		FDIFF-PINN-LSTM	
	MAE	MSE	MAE	MSE	MAE	MSE
0	0.067	0.005	0.079	0.007	0.117	0.017
0.25	0.080	0.007	0.065	0.006	0.080	0.008
0.5	0.081	0.008	0.076	0.006	0.089	0.010
0.75	0.080	0.008	0.094	0.010	0.078	0.010
1	0.072	0.006	0.094	0.013	0.081	0.010
2	0.069	0.006	0.107	0.014	0.081	0.009

**Figure 5.** Analysis of FDIFF-PINN results under different physical weighting coefficients.

Results show:

- **MLP:** Best at $\lambda = 0$ (pure data), performance fluctuates with increasing λ , indicating weak robustness to physical constraints.
- **RNN:** Optimal at $\lambda = 0.25$, with MAE/MSE reducing by 18.3% and 11.8% respectively. Further increasing λ increases error.
- **LSTM:** Optimal at $\lambda = 1$ (MAE=0.0803, MSE=0.00767), with significant error reduction (31.4% MAE, 56.0% MSE) compared to $\lambda = 0$. LSTM effectively fuses physical priors.

4.2.3. Impact of Initial Weights

Table 14 and Table 15 compare the impact of initial weights. Results indicate that initial weights significantly affect accuracy, but PINN models generally show lower errors and better robustness under the same initial weights. For example, at weight 0.01: PINN-MLP reduces MSE by 17.4%; PINN-RNN by 14.6%; PINN-LSTM by 30.5%.

Table 14. Analysis of FDIFF-PINN Results under Different Initial Weights.

Initial Weight	FDIFF-PINN-MLP		FDIFF-PINN-RNN		FDIFF-PINN-LSTM	
	MAE	MSE	MAE	MSE	MAE	MSE
0.001	0.0664	0.0053	0.0866	0.0109	0.0868	0.0100
0.005	0.0682	0.0057	0.0887	0.0117	0.0885	0.0107
0.01	0.0724	0.0064	0.0944	0.0132	0.0946	0.0121
0.05	0.0750	0.0067	0.0979	0.0138	0.0980	0.0126
0.1	0.0778	0.0070	0.1010	0.0144	0.1010	0.0132

Table 15. Analysis of Neural Network Results under Different Initial Weights.

Initial Weight	MLP		RNN		LSTM	
	MAE	MSE	MAE	MSE	MAE	MSE
0.001	0.0735	0.0064	0.0732	0.0062	0.107	0.0143
0.005	0.0755	0.0069	0.0750	0.0067	0.110	0.0154
0.01	0.0802	0.0078	0.0799	0.0075	0.117	0.0174
0.05	0.0830	0.0081	0.0828	0.0079	0.121	0.0182
0.1	0.0861	0.0085	0.0859	0.0082	0.125	0.0190

4.2.4. Impact of Noise Conditions

Experiments assessed robustness against Gaussian and Random noise (intensities 0.05 and 0.1). Table 16 shows MAE and MSE fluctuations are minimal, indicating strong robustness of FDIFF-PINN when noise intensity ≤ 0.1 .

Table 16. Analysis of FDIFF-PINN Results under Different Noise Conditions.

Noise	Level	MLP		FDIFF-MLP	
		MAE	MSE	MAE	MSE
Gaussian	0.05	0.0802	0.00778	0.0724	0.00643
	0.1	0.0802	0.00778	0.0724	0.00643
Random	0.05	0.0815	0.00795	0.0894	0.01000
	0.1	0.0815	0.00793	0.0894	0.01000

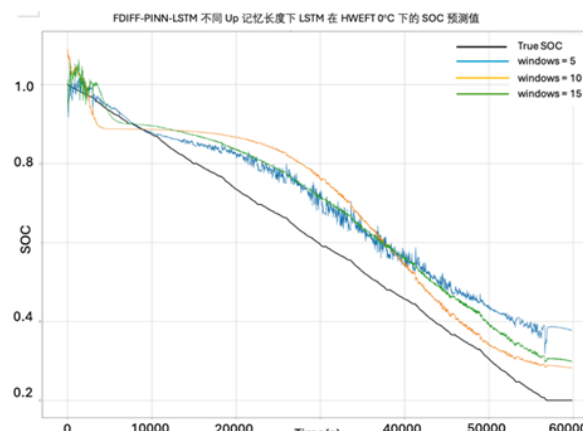
Note: RNN data omitted for brevity but showed similar trends (MAE approx 0.07-0.08).

4.2.5. Impact of Fractional Order Parameters

1) Memory Length Table 17 shows the impact of memory length {5, 10, 15} on RNN and LSTM models. Results indicate nonlinear influence, with longer windows generally enhancing robustness.

Table 17. Analysis of FDIFF-PINN Results under Different Fractional Memory Lengths.

Memory Length	FDIFF-PINN-RNN		FDIFF-PINN-LSTM	
	MAE	MSE	MAE	MSE
5	0.0893	0.0105	0.0950	0.0108
10	0.0944	0.0132	0.0946	0.0121
15	0.0835	0.00818	0.0902	0.00944

**Figure 6.** Analysis of FDIFF-PINN results under different fractional memory lengths.

2) Fractional Order Table 18 shows the impact of fractional order $\alpha \in [0.125, 0.75]$. LSTM shows optimal robustness and smoother SOC curves at $\alpha = 0.125$ and $\alpha = 0.75$.

Table 18. Analysis of FDIFF-PINN Results under Different Fractional Orders.

Fractional Order	FDIFF-PINN-RNN		FDIFF-PINN-LSTM	
	MAE	MSE	MAE	MSE
RNN/LSTM (Ref)	0.0798	0.00754	0.117	0.017
0.125	0.0945	0.0107	0.0793	0.007
0.25	0.0791	0.00778	0.078	0.0071
0.375	0.0829	0.00896	0.093	0.0102
0.5	0.0132	0.0944	0.0802	0.00766
0.75	0.0851	0.00909	0.0637	0.005

4.3. Chapter Summary

This chapter verified the comprehensive advantages of FDIFF-PINN in SOC estimation through series of experiments on initial weights, physical weighting coefficients, noise conditions, and fractional parameters. Comprehensive optimization of physical coefficients, memory length, and model order was performed, with effective validation on the LG18650-HG2 dataset.

5. Conclusions and Outlook

5.1. Conclusions

This study proposed the FDIFF-PINN framework for battery SOC estimation. 1. **Theoretical Advantage:** Fractional derivatives better capture battery relaxation and memory effects than integer-order models. 2. **Effectiveness:** Embedding fractional differential residuals into the loss function successfully regularizes the network. 3. **Performance:** The model reduces SOC estimation error significantly (MSE < 3% in specific conditions) and shows superior robustness at low temperatures.

5.2. Outlook

Future work will focus on: (1) Optimizing model structure for complex conditions; (2) Adaptive hyperparameter tuning using reinforcement learning; (3) Extending to other battery chemistries.

1. Plett, G.L. Extended Kalman Filtering for Battery Management Systems of LiPB-Based HEV Battery Packs—Part 1: Background. *J. Power Sources* **2004**, *134*, 252–261.
2. Plett, G.L. Extended Kalman Filtering for Battery Management Systems of LiPB-Based HEV Battery Packs—Part 2: Modeling and Identification. *J. Power Sources* **2004**, *134*, 262–276.
3. Hu, X.; Li, S.; Peng, H. A Comparative Study of Equivalent Circuit Models for Li-ion Batteries. *J. Power Sources* **2012**, *198*, 359–367.
4. Seaman, A.; Dao, T.-S.; McPhee, J. A Survey of Mathematics-Based Equivalent-Circuit and Electrochemical Battery Models for Hybrid and Electric Vehicle Simulation. *J. Power Sources* **2014**, *256*, 410–423.
5. Lu, L.; Han, X.; Li, J.; Hua, J.; Ouyang, M. A Review on the Key Issues for Lithium-Ion Battery Management in Electric Vehicles. *J. Power Sources* **2013**, *226*, 272–288.
6. Chen, J.; Ouyang, Q.; Xu, C.; Su, H. Neural Network-Based State of Charge Observer Design for Lithium-Ion Batteries. *IEEE Trans. Control Syst. Technol.* **2018**, *26*, 313–320.
7. Li, X.; Zhang, L.; Wang, Z.; Dong, P. Remaining Useful Life Prediction for Lithium-Ion Batteries Based on a Hybrid Model Combining the Long Short-Term Memory and Elman Neural Networks. *J. Energy Storage* **2019**, *21*, 510–518.
8. Wang, S.; Zhao, L.; Su, X.; Ma, P. Prognostics of Lithium-Ion Batteries Based on Battery Performance Analysis and Flexible Support Vector Regression. *Energies* **2014**, *7*, 6492–6508.
9. Dong, H.; Jin, X.; Lou, Y.; Wang, C. Lithium-ion Battery State of Health Monitoring and Remaining Useful Life Prediction Based on Support Vector Regression-Particle Filter. *J. Power Sources* **2014**, *271*, 114–123.

10. Wang, F.; Zhai, Z.; Zhao, Z.; et al. Physics-Informed Neural Network for Lithium-Ion Battery Degradation Stable Modeling and Prognosis. *Nat. Commun.* **2024**, *15*, 4332.
11. Dang, L.; Yang, J.; Liu, M.; Chen, B. Differential Equation-Informed Neural Networks for State of Charge Estimation. *IEEE Trans. Instrum. Meas.* **2023**, *73*, 1000315.
12. Zhong, F.; Li, H.; Zhong, S.; Zhong, Q.; Yin, C. An SOC Estimation Approach Based on Adaptive Sliding Mode Observer and Fractional Order Equivalent Circuit Model for Lithium-Ion Batteries. *Commun. Nonlinear Sci. Numer. Simul.* **2015**, *24*, 127–144.
13. Yang, T.; Li, Y.; Zeng, Y. Secure State of Charge Estimation for Lithium-Ion Batteries under Deception Attacks Based on Attack-Resilient Fractional-Order Extended Kalman Filter. *J. Energy Storage* **2024**, *95*, 112438.
14. Yin, C.; Zhong, S.; Chen, W. Design of Sliding Mode Controller for a Class of Fractional-Order Chaotic Systems. *Commun. Nonlinear Sci. Numer. Simul.* **2012**, *17*, 356–366.
15. Lu, L.; Meng, X.; Mao, Z.; Karniadakis, G.E. DeepXDE: A Deep Learning Library for Solving Differential Equations. *SIAM Rev.* **2021**, *63*, 208–228.
16. Vidal, C.; Kollmeyer, P.; Naguib, M.; Malysz, P.; Gross, O.; Emadi, A. Robust xEV Battery State-of-Charge Estimator Design Using a Feedforward Deep Neural Network. *SAE Int. J. Adv. Curr. Pract. Mobil.* **2020**, *2*.
17. Qayyum, M.; Nayab, S.; Siddique, I.; et al. Analysis of time-fractional cancer-tumor immunotherapy model using modified He-Laplace algorithm. *Sci Rep* **2025**, *15*, 8929.
18. Chen, J.; Gu, W.; Zhang, P.; et al. Fractional Order Viscoelastic Finite Element and Its Application in Surrounding Rock Deformation. *J. Huaiyin Inst. Technol.* **2019**, *28*, 1–4.
19. Hafez, I.; Wadi, A.; Abdel-Hafez, M.F.; Hussein, A.A. Variational Bayesian Based Maximum Correntropy Cubature Kalman Filter Method for State-of-Charge Estimation of Li-ion Battery Cells. *IEEE Trans. Veh. Technol.* **2022**, *72*, 3090–3104.
20. Xiong, R.; He, H.; Sun, F.; Zhao, K. Evaluation on State of Charge Estimation of Batteries with Adaptive Extended Kalman Filter by Experiment Approach. *IEEE Trans. Veh. Technol.* **2012**, *62*, 108–117.
21. El Din, M.S.; Hussein, A.A.; Abdel-Hafez, M.F. Improved Battery SOC Estimation Accuracy Using a Modified UKF with an Adaptive Cell Model Under Real EV Operating Conditions. *IEEE Trans. Transp. Electrif.* **2018**, *4*, 408–417.
22. Tang, X.; Zou, C.; Yao, K.; Lu, J.; Xia, Y.; Gao, F. Aging Trajectory Prediction for Lithium-Ion Batteries via Model Migration and Bayesian Monte Carlo Method. *Appl. Energy* **2019**, *254*, 113591.
23. Tan, Y.; Zhao, G. Transfer Learning with Long Short-Term Memory Network for State-of-Health Prediction of Lithium-Ion Batteries. *IEEE Trans. Ind. Electron.* **2020**, *67*, 8723–8731.
24. Shen, S.; Sadoughi, M.; Li, M.; Wang, Z.; Hu, C. Deep Convolutional Neural Networks with Ensemble Learning and Transfer Learning for Capacity Estimation of Lithium-Ion Batteries. *Appl. Energy* **2020**, *260*, 114296.